COBEM 2023 27TH INTERNATIONAL CONGRESS OF MECHANICAL ENGENEERING

ABCM Brazilian Society of Mechanical Sciences and Engineering
27th ABCM International Congress of Mechanical Engineering
December 04-08, 2023, Florianópolis-SC, Brazil

COB-2023-0719
EVALUATION OF SHEAR-THINNING AND SHEAR-THICKENING FLUIDS APPLIED FOR ENHANCED OIL RECOVERY IN HETEROGENEOUS POROUS MEDIUM

Ayrton Cavallini Zotelle
Renato do Nascimento Siqueira
LPMF, Department of Mechanical Engineering, Instituto Federal do Espírito Santo - campus São Mateus, Rod. BR 101 norte, km 58, Litorâneo, São Mateus, ES, 29932-540, Brazil
ayrton.zotelle@ifes.edu.br
renatons@ifes.edu.br

Edson José Soares
LABREO, Department of Mechanical Engineering, Universidade Federal do Espírito Santo, Avenida Fernando Ferrari, 514, Goiabeiras, Vitória, ES, 29075-910, Brazil
edson.soares@ufes.br

Abstract. *The increase of the fraction of extracted oil in petroleum reservoirs is one of the greatest challenges of the petroleum industries, since the oil corresponds to one of the most important energy resources. One of the most useful methods to increase the oil recovery is the injection of a fluid on the reservoir to displace the oil. The primary motivation of this work is to evaluate the liquid-liquid displacement on a heterogeneous porous medium using the Computational Fluid Dynamics (CFD). The Basilisk© software is an open source code used to solve complex flows, in special those with interfacial phenomena. The porosity of the porous medium is* $\phi = 0.7$*, the range of evaluated viscosity ratio* $0.2 \leq N_\mu \leq 40$ *and capillary number* $0.02 \leq Ca \leq \infty$*. The injected fluid has Newtonian, shear-thinning and shear-thickening characteristics with Power-Law index range* $0.5 \leq n \leq 1.5$*. It is observed that while the viscosity ratio decreases, the amount residual oil that remains trapped in the porous media reduce due to the increase of the shear-stress imposed by the injected fluid. For* $N_\mu > 1$*, the increase in the interfacial tension makes the interface flat, assisting the displacement , while for* $N_\mu < 1$*, the increase of the interfacial tension reduces the sweep on minor pores, so, more of the recovered fluid is left behind. The Pseudo-plasticity was evaluated at low interfacial tension. It was observed that the shear-thinning fluid recovers more fluid than the Newtonian or shear-thickening fluids. Due to the tendency of the injected fluid to pass through the largest pores, the velocity and consequently the shear-rate on minor pores is low, contributing to the increase in the local viscosity of the shear-thinning fluid and also increasing its capability to displace the oil.*

Keywords: *Enhanced Oil Recovery. Viscosity ratio. Capillary number. Shear-thinning fluid. Shear-thickening fluid.*

1. INTRODUCTION

Petroleum is a mixture of hydrocarbons that is produced and stored in the subsoil, inside porous rocks, called reservoirs. Those rocks may be constituted of various materials, but to be considered reservoirs, they may have voids in their structure, where the oil will be stored. To reach the petroleum, it is necessary to drill a well to connect the reservoir with the surface and produce the oil. The petroleum corresponds to one of the main sources of energy. According to the Brazilian Energy Balance, the energy originated from petroleum and derivatives corresponds to 34.4% of the total energy supply, leading to a production of $170.000.000\ m^3$ in 2021. In the year of 2001, the Brazilian oil production was $80.000.000\ m^3$, indicating a growth of 212.5% on the internal production in 20 years (EPE, 2022).

Due to the increase in the national oil production, new technologies and methods were developed to increase the petroleum exploration to meet the demand of world consumption of oil (Muggeridge *et al.*, 2014). The oil recovery occurs typically in three stages. In the initial oil production (primary recovery stage), the oil is produced by the internal energy of the reservoir, i.e., the well has enough pressure to lift the oil from the reservoir to the surface. During production, the internal pressure of the reservoir reduces, and also the rate of oil production, in a process called "well depletion" (Thomaz, 2001; Chavent *et al.*, 2014). Only around $20 - 30\%$ of the total oil is recovered in this stage, remaining a considerable fraction of the total oil in the reservoir (Tunio *et al.*, 2011).

To cope with the loss of productivity on the primary recovery stage, the petroleum industry developed the secondary and tertiary recovery processes. These processes consist in artificial oil elevation. A fluid is injected into the reservoir to displace the oil, to take its place in the pores of the reservoir, maintaining the well pressure. On the secondary stage, normally the displacement is made by water or gas injection. The residual oil that remains trapped in the porous after the

secondary stage is significant, on average, more than 60% of the original oil in the geological reservoir (Tunio *et al.*, 2011). In the third stage of the oil production, also called enhanced oil recovery (EOR), it is common to use polymer solutions or surfactants after water-flooding, which can recover a significant additional amount of oil (Needham and Doe, 1987; Fathi *et al.*, 2011). The polymeric solutions turn the injected fluid more viscous, or even give to it non-Newtonian characteristics that may help the displacement process. On average, the EOR can reach the recovery of $60 - 65\%$ of the original reservoir volume.

Depending on the characteristics of the injected fluid and the oil, and also some operational parameters and characteristics of the reservoir, the interfacial dynamics of the fluid-fluid-solid can be completely affected, improving or impairing the oil displacement. An example is the formation of preferential paths to the injected fluid passage, called fingers, failing to displace most of the oil and reducing the recovery efficiency. The interface pattern is strongly affected by parameters such as the viscosity ratio between the recovered and the injected fluid (N_μ), the interfacial tension, evaluated thought the Capillary number (Ca) and the characteristics of the porous medium (such the homogeneity or disorder). From this view, this work evaluates the influence of Ca, N_μ, shear-thinning and shear-thickening behavior (using the Carreau-Yasuda model) on the displacement efficiency of a fluid on a heterogeneous porous medium.

2. MATHEMATICAL FORMULATION

This paper uses the Basilisk© software to simulate a multiphase interaction between two fluid phases and one solid phase on a recovery process in a porous media. The fluids and solid interaction were modelled using the embedded boundary method (more details at Johansen and Colella (1998)). The fluids interaction was modelled using the Volume of Fluid (VOF). This model treats the phases as continuous and immiscible, solving a unique continuity and momentum equation for both the phases, also called one-fluid method, and tracks the interface around the domain by solving the advection equation to the volume fraction (f) of the primary phase:

$$\frac{\partial f}{\partial t} + \boldsymbol{u} \cdot \nabla f = 0 \,, \tag{1}$$

in which $\boldsymbol{u}$ is the velocity vector. The mass also needs to be conserved in the flow. Considering an incompressible flow, the continuity equation to a one-fluid method is:

$$\nabla \cdot \boldsymbol{u} = 0 \,, \tag{2}$$

in which $\boldsymbol{u}$ is the velocity field and the momentum equation, considering the multiphase flow with the surface tension source interaction is:

$$\rho \left(\frac{\partial \boldsymbol{u}}{\partial t} + \boldsymbol{u} \cdot \nabla \boldsymbol{u} \right) = -\boldsymbol{\nabla} P + (\rho_1 - \rho)\, \boldsymbol{g} + \nabla \cdot \left[\mu \left(\nabla \boldsymbol{u} + \nabla \boldsymbol{u}^T \right) \right] + \boldsymbol{S}_\sigma \,, \tag{3}$$

where P is the pressure field and $\boldsymbol{S}_\sigma$ is the source term due to the interfacial forces. The fluid properties are calculated considering the fraction of each fluid on the numerical cell. The density is calculated by the average mass on the mesh:

$$\rho = f\rho_1 + (1 - f)\rho_2 \,. \tag{4}$$

The subscripts 1 and 2 refers to the fluid to be displaced and the injected fluid, respectively. The viscosity field was calculated by a harmonic mean of the viscosity:

$$\mu = \frac{1}{\frac{f}{\mu_1} + \frac{(1-f)}{\eta_2(\dot{\gamma})}}. \tag{5}$$

The viscosity of the injected fluid ($\eta_2(\dot{\gamma})$) depends on the fluid rheology. For a Newtonian scenario, the viscosity is constant $\eta(\dot{\gamma}) = \mu_2$. For the shear-thinning and shear-thickening simulations, the rheology of the injected fluid was modelled using the Carreau-Yasuda model. The model presents two Newtonian plateaus η_0 and η_∞, when $\dot{\gamma} \to 0$ and $\dot{\gamma} \to \infty$, respectively. The general expression for the Carreau-Yasuda model is expressed by:

$$\eta_2(\dot{\gamma}) = \eta_\infty + (\eta_0 - \eta_\infty) \left[1 + (\lambda_{CY}\dot{\gamma})^a \right]^{\frac{n-1}{a}} \,. \tag{6}$$

$\dot{\gamma}$ is the shear-rate intensity, and a and λ_{CY} are parameters of the model to be adjusted, and n is the Power-Law index, that controls the shear-thinning or shear-thickening behavior of the fluid. For $n < 1$, the fluid is shear-thinning and for $n > 1$ the fluid is shear-thickening.

2.1 Modelling surface tension

The surface tension is simply a force per unit length, tangential to the curve section, which can be expressed as:

$$\boldsymbol{F_\sigma} = \int_L \sigma\, \boldsymbol{m}\, dl\ , \tag{7}$$

in which σ is the interfacial tension, $\boldsymbol{m}$ is the cross-section tangent vector and dl a length increment along the curve L, as shown in Fig. 1.

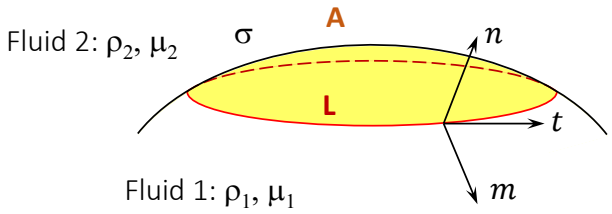

Figure 1: Representation of an interface between two arbitrary fluids.

Using the Stokes Theorem, we can convert the length force into a surface force:

$$\int_L \sigma\, \boldsymbol{m}\, dl\ = \int_A [\nabla\sigma + \sigma(\nabla\cdot\boldsymbol{n})\boldsymbol{n}]\, da\ . \tag{8}$$

In a constant surface tension model, the first term in the right hand of Eq. 8 is equal to 0. Note that the term $\nabla\cdot\boldsymbol{n}$ represents the interface curvature (κ), i.e.:

$$\boldsymbol{F_\sigma} = \int_A \sigma\kappa\boldsymbol{n}\, da\ . \tag{9}$$

We can also convert the surface force into a volumetric force using Gauss theorem:

$$\int_A \sigma\kappa\boldsymbol{n}\, da\ = \int_V \sigma\kappa\delta_d\boldsymbol{n}\, dv\ , \tag{10}$$

in which δ_d is the Dirac delta function, that is zero in all zones of the numerical domain, except on the fluids interface. Therefore, the source term $\boldsymbol{S}_\sigma$, that corresponds to the interfacial force per unit of volume is:

$$\boldsymbol{S}_\sigma = \sigma\kappa\delta_d\boldsymbol{n}\ . \tag{11}$$

The normal vector n is calculated using the volume fraction (f) of the primary phase:

$$\boldsymbol{n} = \frac{\nabla f}{|\nabla f|}\ . \tag{12}$$

The Dirac delta function, δ_d, is used to locate the interface. δ_d was calculated using the continuous surface force method (CSF), that calculates the interface tracking function as:

$$\delta_d = |\nabla f|. \tag{13}$$

Note that Eq. 13 is indeed a consistent approximation of a Dirac delta function, according to Brackbill *et al.* (1992) and Popinet (2018).

2.2 Dimensionless governing equation

The physical interpretation of a complex phenomenon involves plenty of variables, turning the interpretation of the results quite complex. To overcome these difficulties, the dimensionless analyses help to reduce the quantity of variables of the problem, and help to compare results of the literature even with different geometries and operational parameters. In a flow through a porous medium, the dimensionless parameters are:

$$\boldsymbol{u}' = \frac{\boldsymbol{u}}{U};\ \ \rho' = \frac{\rho}{\rho_1};\ \ \mu' = \frac{\mu}{\mu_1};\ \ t' = t\frac{\mu_1}{\rho_1\phi k};\ \ P' = P\frac{\sqrt{\phi k}}{\mu_1 U};\ \ \nabla' = \sqrt{\phi k}\nabla;\ \ \kappa' = \sqrt{\phi k}\kappa;\ \ \delta_d' = \sqrt{\phi k}\delta_d\ , \tag{14}$$

where U is the Darcy velocity, ϕ is the porous medium porosity and k is the absolute permeability of the porous medium. Using the dimensionless parameters of Eq. 14 on Eq. 3 and replacing the surface tension source term ($\boldsymbol{S}_\sigma$) by Eq. 11, we find the dimensionless momentum equation for a flow through a porous medium:

$$\left[f+(1-f)\frac{1}{N_\rho}\right]\left(\frac{\partial \boldsymbol{u}'}{\partial t'}+Re\,\boldsymbol{u}'\cdot\nabla'\boldsymbol{u}'\right)=-\boldsymbol{\nabla}'P'+\nabla'\cdot\left[\frac{1}{f+(1-f)\frac{N_\mu}{\epsilon(\dot\gamma)}}\left(\nabla'\boldsymbol{u}'+\nabla'\boldsymbol{u}'^{T}\right)\right]+\frac{1}{Ca}\kappa'\delta_d'\boldsymbol{n}\,, \tag{15}$$

in which $Re=\rho_1 U\sqrt{k}/\mu_1$ is the Reynolds number, $Ca=\sigma U/\mu_1$ is the capillary number, $N_\rho=\rho_1/\rho_2$ is the density ratio and $N_\mu=\mu_1/\eta_c$ is the viscosity ratio. $\eta_c=\eta_2(\dot\gamma_c)$ is the injected fluid characteristic viscosity and the characteristic shear-stress ($\dot\gamma_c$) is:

$$\dot\gamma_c=\frac{(3n+1)}{4n}\frac{U}{\sqrt{\phi k}}\,. \tag{16}$$

We study the specific case that $N_\rho=1$ and $Re<<1$ (Creeping flow). Therefore, the dimensionless momentum equation can be overwritten as:

$$\frac{\partial \boldsymbol{u}'}{\partial t'}=-\boldsymbol{\nabla}'P'+\nabla'\cdot\left[\frac{1}{f+(1-f)^{N_\mu/\epsilon(\dot\gamma)}}\left(\nabla'\boldsymbol{u}'+\nabla'\boldsymbol{u}'^{T}\right)\right]+\frac{1}{Ca}\kappa'\delta_d'\boldsymbol{n}\,, \tag{17}$$

where the term:

$$\epsilon(\dot\gamma)=\frac{1+(N_{CY}-1)\left[1+(\lambda_{CY}\dot\gamma)^a\right]^{\frac{n-1}{a}}}{1+(N_{CY}-1)\left[1+(\lambda_{CY}\dot\gamma_c)^a\right]^{\frac{n-1}{a}}}\,, \tag{18}$$

represents the ratio $\eta(\dot\gamma)/\eta_c$, where $N_{CY}=\eta_0/\eta_\infty$. The term of Eq. 18 introduces the shear-rate dependence of the shear-thinning or shear-thickening fluid on the two-phase fluid flow, and the fraction $N_\mu/\epsilon(\dot\gamma)$ represents the local viscosity ratio. It is noted that if the Power-Law index $n=1$, $\epsilon(\dot\gamma)=1$ for the entire range of shear-rate.

3. METHODOLOGY

The numerical model evaluated is a simplified 2D microscale porous media and was used to study the influence of the viscosity ratio (N_μ), the capillary number (Ca) and the power-law index (n) on recovery efficiency. The geometry is a heterogeneous porous medium with random position and grain size based on the study of Mora *et al.* (2021), as show Fig. 2.

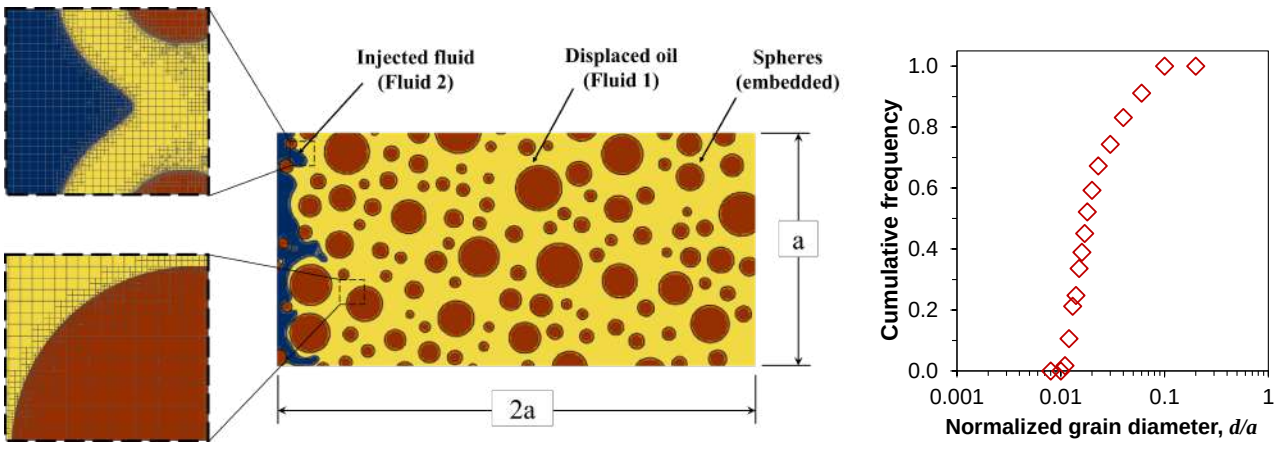

(a) (b)

Figure 2: Parameters of the numerical domain (a) porous medium geometry and (b) cumulative grain size distribution.

Initially, the domain is fully saturated with the fluid to be displaced (yellow on Fig. 2a). The injected fluid (blue on Fig. 2a), flows from the left to the right with a flow rate that corresponds to a characteristic shear-rate $\dot\gamma_c=10\ s^{-1}$, ensuring a Reynolds number $Re<10^{-3}$. The characteristic shear rate corresponds to typical shear rates in the oil reservoirs (Nilsson *et al.*, 2013). The right section has relative pressure $0\ Pa$, the top and bottom section, the free slip condition is applied, and the spheres (brown) were simulated with no-slip condition, modelled with the embedded boundary (more details in Johansen and Colella (1998) and Limare *et al.* (2022)). The dimensionless absolute permeability of the porous medium corresponds to ${}^{k}/_{a^2}=0.0019$, and the porosity was $\phi=0.7$.

The Basilisk© software is an open-source code to solve differential partial equations using the Finite Volume Method (FVM) developed at Centre National de la Recherche Scientifique (CNRS) based at Institut Jean le Rond ∂'Alembert of Sorbonne Université, Paris - France (Popinet, 2009, 2015; Lagrée *et al.*, 2011). This software has been used for various flows, especially those with interfacial dynamics, by different researchers (Lagrée *et al.*, 2011; Deike *et al.*, 2015, 2016; Deka *et al.*, 2019; Pierson *et al.*, 2020; Deka *et al.*, 2020; Deoclecio *et al.*, 2021; Limare *et al.*, 2022; Farsoiya *et al.*, 2022). The solver uses Cartesian Meshes, which can be refined on critical regions. In this study, the mesh is adapted on the regions with volume fraction gradients (∇f) to a better interface representation, on the fluids-solid interface, i.e., on the embedded boundary (left on Fig.2a), on zones with high velocity gradient ($\nabla \boldsymbol{u}$) and, to the non-Newtonian cases, the mesh is also adapted to the viscosity gradient ($\nabla \mu$).

Explicit schemes for the transport of interfaces are subject to the standard Courant–Friedrichs–Lewy constraint, or Courant number:

$$Co = \frac{|\boldsymbol{u}|\Delta t}{\Delta} \,, \tag{19}$$

in which u is the local mesh velocity, Δ is the local mesh length and Δt is the time-step size. The Courant number represents the advective flux that crosses the mesh volumes in a given time interval. The fraction between the local mesh size and the local velocity is also called advective time-step, $\Delta t_{adv} = \Delta/|\boldsymbol{u}|$, it means that:

$$Co = \frac{\Delta t}{\Delta t_{adv}} \,. \tag{20}$$

To the numerical stability, the Courant–Friedrichs–Lewy constraint implies $Co \leq 0.5$. A time-explicit discretization of the surface tension term should lead to a stability constraint, so the maximum time-step needs to be smaller than the oscillation period of the smallest capillary wave ($\Delta t \leq \Delta t_\sigma$) (Brackbill *et al.*, 1992; Galusinski and Vigneaux, 2008; Popinet, 2018), where the oscillation period of the smallest capillary wave (Δt_σ) is:

$$\Delta t_\sigma = \sqrt{\frac{(\rho_1 + \rho_2)\Delta^3}{2\pi\sigma}} \,. \tag{21}$$

The ratio of these two stability constraints is:

$$\frac{\Delta t_\sigma}{\Delta t_{adv}} = \sqrt{\frac{(\rho_1 + \rho_2)|\boldsymbol{u}|^2\Delta}{2\pi\sigma}} = \sqrt{\frac{We_\Delta}{\pi}} \,, \tag{22}$$

where We_Δ is the cell Weber number, which estimates the ratio of inertial to surface tension forces on the cell mesh (Popinet, 2018). This means that, for a well solved simulation with $We_\Delta << 1$, the capillary time-step restriction (Δt_σ) must always be more restrictive than the Courant–Friedrichs–Lewy constraint for interface advection.

Most of the results were analyzed at the breakthrough time, that corresponds to the moment in which the injected fluid reaches the outlet section. The recovered fluid is Newtonian in all simulated cases, while different rheologies were applied to the injected fluid (Newtonian, shear thinning and shear-thickening) and the density ratio $N_\rho = 1$ in all cases. The Newtonian cases were performed as a comparative parameter to verify the effects of each rheology on the fluid interface. Another usual parameter to verify the dimensionless groups effects on the displacement efficiency is the lost mass fraction (m_e), that corresponds to the fraction of recovered fluid at the breakthrough time divided by the mass of fluid inside the porous medium at the beginning of the displacement:

$$m_e = \frac{\sum(f\Delta^2)}{\sum(\Delta^2)} \,. \tag{23}$$

The transient development of the interface was also evaluated to investigate the effects of the viscosity ratio on the displacement behavior, while the capillary number was fixed ($Ca = \infty$). The development was evaluated as a function of the injected porous volume (V_ϕ), which represents the volume of the injected fluid by the volume of the porous medium:

$$V_\phi = \frac{Qt_i}{V_p} \,, \tag{24}$$

where Q is the flow rate, t_i is the time elapsed since the beginning of the simulation, and V_p is the porous volume. Equation 24 is valid for displacements at a fixed flow rate. In the Newtonian cases, the viscosity ratio ranges from $N_\mu = 0.2$ to $N_\mu = 40$ and the capillary numbers range from $Ca = 0.01$ to $Ca = \infty$ (no surface tension, $\sigma = 0$). To the non-Newtonian scenarios, some specific values of viscosity ratio were chosen ($N_\mu = 20; 10; 4; 0.5$) and the Capillary number effects were isolated, i.e., all the simulations of the non-Newtonian cases were performed at high Capillary number ($Ca = \infty$). The shear-thinning fluid simulations were performed for Power-Law index (n) ranging from 0.5 to 0.9 with the step of 0.1 and the shear-thickening fluid from 1.1 to 1.5 with the same step. The other parameters of the Carreau-Yasuda model were kept constant.

4. RESULTS AND DISCUSSIONS

4.1 Influence of viscosity ratio and capillary number on displacement patttern

Figure 3 shows the interface of the injected fluid at the breakthrough time for the viscosity ratio values $N_\mu = 20; 10; 4; 1$ and 0.5 and $Ca = \infty; 1$ and 0.02.

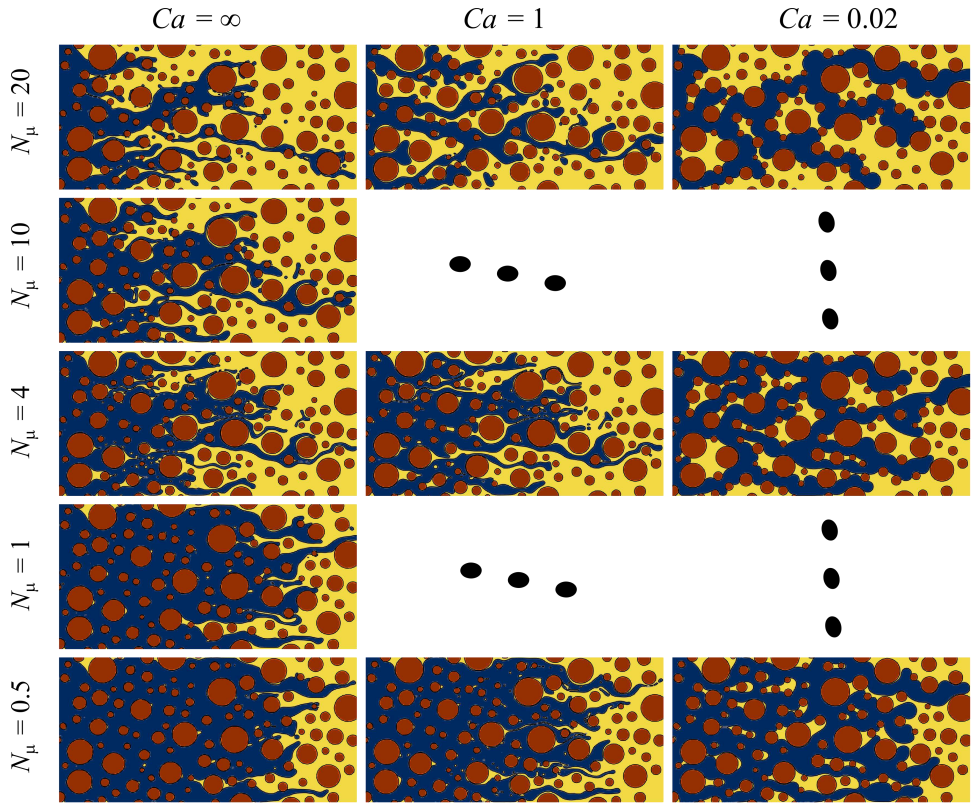

Figure 3: Influence of Viscosity ratio (N_μ) and Capillary number (Ca) on displacement pattern at the breakthrough time.

Observing the first column of Fig. 3, where the interface tension effects are negligible, it is possible to see that the entrapped liquid decreases when N_μ decreases, i.e., when the viscosity of the injected fluid increases. The amount of liquid on the domain is significant for $N_\mu = 20$ and almost absent for $N_\mu = 0.5$, becoming evident that the formation of the preferential paths is hardly dependent on viscosity ratio. Specially at a low viscosity ratio, the injected fluid displaces more fluid than in the case of a high viscosity ratio, as would be expected for stable or near-stable displacement of a less viscous fluid by a much more viscous fluid at a high Ca. This was also investigated on a homogeneous porous medium by Zhang *et al.* (2011). The improvement of recovery efficiency obtained with a reduction of N_μ occurs due to the increase in the viscous drag imposed by the high viscosity of the injected fluid at low N_μ. This behavior was also observed by some studies in capillary tubes (Taylor, 1960, 1961; Soares *et al.*, 2005; Soares and Thompson, 2009; Soares *et al.*, 2015; Caliman *et al.*, 2017) and studies on porous media (Lenormand *et al.*, 1988; Zhang *et al.*, 2011; Gu *et al.*, 2018; Liu *et al.*, 2013).

Fixing the viscosity ratio, it is possible to note that while the Capillary number decreases, i.e., an increase in the relative importance of interface tension, the viscous and capillary forces influence the displacement. Let us evaluate the case with $N_\mu = 20$ and $Ca = 0.02$. To minimize the surface force, with the increase in the interfacial tension (σ), the interface curvature (κ) may reduce. Therefore, the interface becomes flat, with the decrease of Ca, resulting in an increase in the flow path width and, consequently, the entrapped liquid decreases. This behavior is the same observed numerically and experimentally by Soares and Thompson (2009); Soares *et al.* (2015) and Caliman *et al.* (2017) on capillary tubes.

When the interfacial tension increases, larger blobs of the displaced fluid are trapped by the injected fluid, and the injected fluid flows into the large pores more easily due to higher capillary pressure (Gu *et al.*, 2018). An interesting effect occurs for $N_\mu = 0.5$, with the increase in the interfacial tension (reducing Ca), the injected fluid interface can be flat inside some pores, i.e., the injected fluid does not pass through some pores that were invaded for $Ca = \infty$, though most interfaces remain curved due to large capillary pressure (Gu *et al.*, 2018). In the capillary fingers pattern, the fluid preferentially passes through the largest pore because the capillary pressure becomes high on minor pores. Meanwhile, much more of the fluid to be displaced is left behind as the injected phase continues to move forward. This is evident, comparing the scenarios to $Ca = \infty$ and $Ca = 0.02$ for $N_\mu = 0.5$.

Figure 4 shows the results of the influence of the viscosity ratio (N_μ) and capillary number (Ca) on the lost mass fraction (m_e).

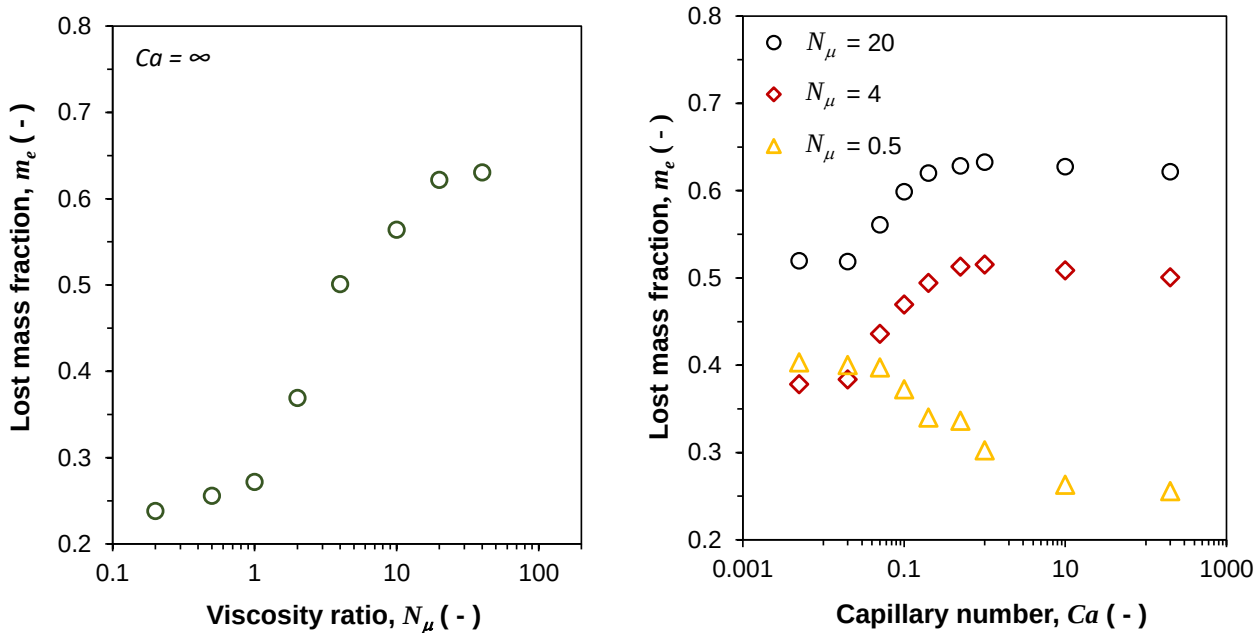

(a) (b)

Figure 4: Influence of (a) Viscosity ratio, N_μ and (b) Capillary number, Ca, on the lost mass fraction m_e.

As shown in Fig. 4a, when the relative importance of Ca is absent, the lost mass fraction presents an asymptotic behavior as a function of the viscosity. The lost mass fraction presents low variation for $N_\mu > 20$, which is in accordance with the studies of Gu *et al.* (2018). As the viscosity ratio decreases for $N_\mu \leq 20$ the lost mass fraction starts to present a substantive variation with the decrease of N_μ. These phenomena are in accordance with the literature (Lenormand *et al.*, 1988; Soares *et al.*, 2005; Soares and Thompson, 2009; Zhang *et al.*, 2011; Liu *et al.*, 2013).

When the viscosity ratio is higher than 20, the shear stress imposed by the injected fluid is too low compared with the shear stress of the recovered fluid. Therefore, the displacement occurs not due to the viscous drag, but by the interface front displacement through the porous media, making the injected fluid inefficient to displace the fluid, so, there is no significant changes to the lost mass fraction for $N_\mu > 20$ on Fig. 4a. The reduction of the lost mass fraction for $N_\mu \leq 20$ is due to the increase in the shear stress imposed by the injected fluid, increasing the viscous drag, while the ratio of the fluid viscosity decreases, permitting the injected fluid to sweep the pores with a high efficiency. Reducing N_μ even more, the lost mass fraction reaches another asymptotic plateau, for low viscosity ratios. In this scenario, the displacement occurs mostly by the viscous drag, which is high enough to displace a large amount of oil.

It is observed in Fig. 4b that the increase of Ca also increases m_e at $N_\mu = 20$ and 4, until it reaches an asymptotic plateau. For $N_\mu > 1$, a flat interface displaces more fluid than a sharp one. Therefore, the displacement with a low Ca is more efficient than for high values of Ca. This behavior has the same tendency observed in the literature for capillary tubes and porous medium (Taylor, 1960, 1961; Soares *et al.*, 2005; Soares and Thompson, 2009; Soares *et al.*, 2015; Caliman *et al.*, 2017). But analyzing the lost mass fraction behavior for $N_\mu = 0.5$, it is observed that it increases with the reduction of Ca. The interfacial tension forces reduce the injected fluid penetration in the smallest pores, reducing the capability to displace the recovered fluid on those regions, i.e., for low viscosity ratio, the increase of Ca also increases the displacement efficiency. This behavior is in accordance with other studies in porous medium (Lenormand *et al.*, 1988; Zhang *et al.*, 2011).

4.2 Influence of Power-Law index on displacement pattern

The non-Newtonian simulations were performed, evaluating only the viscous effects on the displacement. Therefore, the Capillary number was fixed $Ca = \infty$, so the interfacial tension effects are negligible. Figure 5 illustrates the fluids interface pattern, comparing the Newtonian case with the most shear-thinning case ($n = 0.5$) and the most shear-thickening case ($n = 1.5$).

For high viscosity ratios ($N_\mu = 20; 10$), it is noted that the fluid rheology does not have a strong influence on the fluids interface. However, for $N_\mu = 0.5$ the changes on the interfaces are evident, compared to shear-thickening and the Newtonian case. Interesting to note that there were no significant changes to the fluid interface for the Newtonian and shear-thinning cases. The Newtonian case, for this viscosity ratio, drags the majority of the fluid to be displaced, and

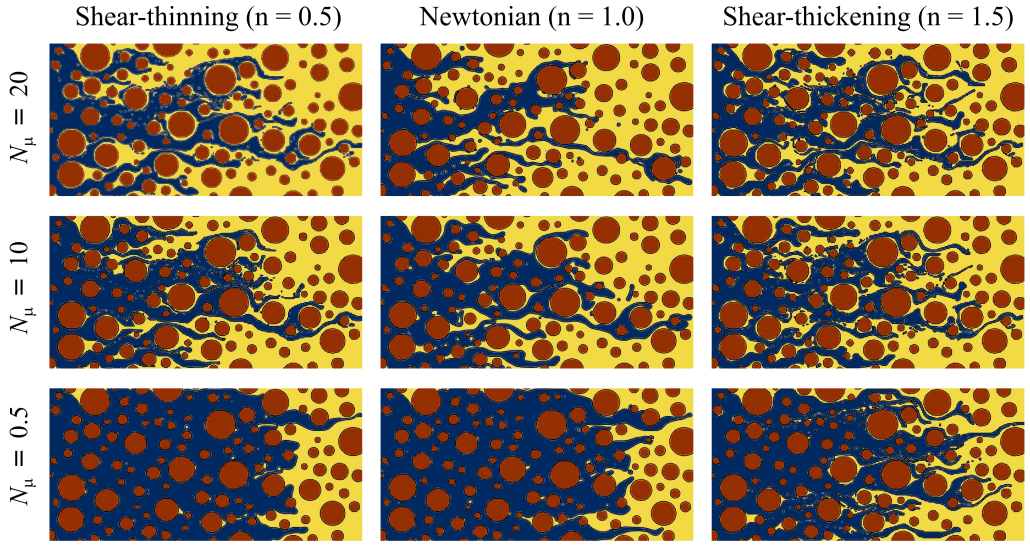

Figure 5: Influence of the Power-Law index (n) on the fluid interface pattern at the breakthrough time.

there is almost no liquid film on the grains of the porous medium, indicating that the flow pattern is stable or near stable. Therefore, the increase in the drag forces due to the shear-thinning behavior does not change the fluid interface. Figure 6 shows the lost mass fraction for a range of Power-Law index (n) for the viscosity ratios $N_\mu = 20; 10; 4$ and 0.5.

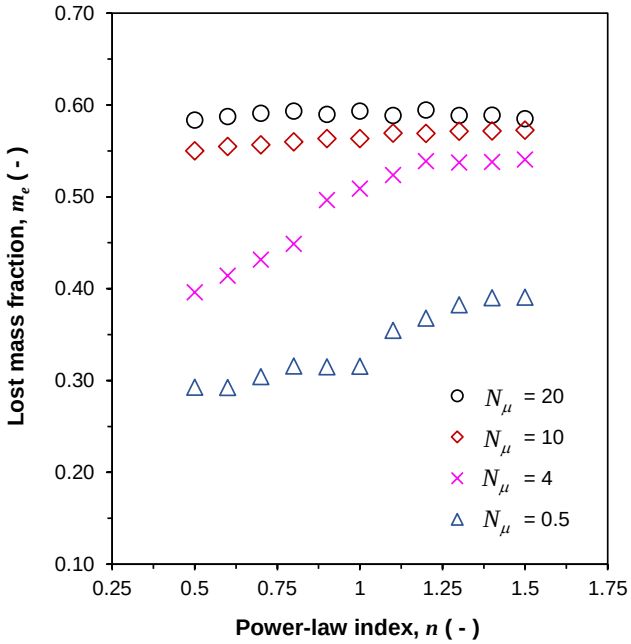

Figure 6: Influence of the Power-Law index (n) on the lost mass fraction (m_e) for $N_\mu = 20$, 10, 4 and 0.5.

It is possible to see in Fig. 6 that the fluid rheology only significantly affects the lost mass fraction m_e for the viscosity ratio $N_\mu = 4$ and 0.5, been almost constant for $N_\mu = 20$ and 10 for the entire range of Power-Law index. It is noted that for $N_\mu = 4$, the lost mass fraction is strongly affected by n for the shear-thinning range, while for $N_\mu = 0.5$, there are no significant changes. As discussed before, the flow pattern for $N_\mu = 0.5$ and $n = 1$ (Newtonian) is stable or near stable. So, the increase of the shear-stress as n decreases, do not affect the lost mass fraction. The opposite occurs for $N_\mu = 0.5$ and $n > 1$, it is seen that the lost mass fraction has an increase from the Newtonian to the shear-thickening case, indicating a reduction of the shear-stress imposed by the injected fluid, destabilizing the interface front. For $N_\mu = 4$ the shear-thinning behavior is quite important to reduce m_e, at Power-Law indexes $n \geq 1.2$, the lost mass fraction reaches a constant plateau. The increase of n for $N_\mu = 4$ makes the displacement more unstable, reducing the shear-stress imposed by the injected fluid and making the displacement more close to the viscous finger patterns. It was noted that the tendency is to reduce the lost mass fraction while the fluid becomes shear-thinning. Those results disagree with the study of Nilsson *et al.* (2013), but are in agreement with other studies in the literature (de Sousa *et al.*, 2007; Thompson and Soares, 2012; de Castro *et al.*, 2016; Zamani *et al.*, 2019; Shende *et al.*, 2021; Salmo *et al.*, 2020, 2021).

5. CONCLUSIONS

This study evaluates the immiscible liquid-liquid displacement in heterogeneous porous medium by Newtonian and non-Newtonian fluids, analyzing the effects of the capillary number, viscosity ratio and Power-Law index on the lost mass fraction and fluids interface. For values of viscosity ratio $N_\mu > 1$, it was verified that the increase in the capillary number (Ca), helps with the displacement by making the interface of the fluids flat. Another possibility to increase the displacement of the fluid in the porous media is to introduce the shear-thinning characteristics of the fluids, that increase the shear-stress imposed by the injected fluid, also increasing the fraction of recovered oil. For $N_\mu < 1$, the displacement is also stable. Therefore, by increasing the capillary number, it is possible to interfere on the swept, increasing the displacement. The shear-thinning behavior does not significant affect the lost mass fraction for $N_\mu < 1$. Therefore, for low values of viscosity ratio, operating by with high capillarity and no shear-thinning behavior represents the ideal scenarios. The combined characteristics of n and Ca were not evaluated for the range of viscosity ratio to evaluate the mos ideal scenarios to realize the recovery process. Consequently, the next steps of this study are to evaluate this combination and also other rheological models, such as viscoplastic and viscoelastic fluids.

6. ACKNOWLEDGEMENTS

The authors thank the Instituto Federal do Espírito Santo (IFES) and the Universidade Federal do Espírito Santo (UFES) for the resources to carry the research and FAPES for the financial support for the development of this research.

7. REFERENCES

Brackbill, J., Kothe, D. and Zemach, C., 1992. "A continuum method for modeling surface tension". *Journal of Computational Physics*, Vol. 100, No. 2, pp. 335–354. doi:10.1016/0021-9991(92)90240-y.

Caliman, H.M., Soares, E.J. and Thompson, R.L., 2017. "An experimental investigation on the newtonian–newtonian and viscoplastic–newtonian displacement in a capillary tube". *Journal of Non-Newtonian Fluid Mechanics*, Vol. 247, pp. 207–220. doi:10.1016/j.jnnfm.2017.08.001.

Chavent, G., Jaffr, J. and Jaffre, J., 2014. *Mathematical models and finite elements for reservoir simulation*. Studies in Mathematics and Its Applications. North-Holland.

de Castro, A.R., Oostrom, M. and Shokri, N., 2016. "Effects of shear-thinning fluids on residual oil formation in microfluidic pore networks". *Journal of Colloid and Interface Science*, Vol. 472, pp. 34–43. doi:10.1016/j.jcis.2016.03.027.

de Sousa, D.A., Soares, E.J., de Queiroz, R.S. and Thompson, R.L., 2007. "Numerical investigation on gas-displacement of a shear-thinning liquid and a visco-plastic material in capillary tubes". *Journal of Non-Newtonian Fluid Mechanics*, Vol. 144, No. 2-3, pp. 149–159. doi:10.1016/j.jnnfm.2007.03.006.

Deike, L., Melville, W.K. and Popinet, S., 2016. "Air entrainment and bubble statistics in breaking waves". *Journal of Fluid Mechanics*, Vol. 801, pp. 91–129. doi:10.1017/jfm.2016.372.

Deike, L., Popinet, S. and Melville, W.K., 2015. "Capillary effects on wave breaking". *Journal of Fluid Mechanics*, Vol. 769, pp. 541–569. doi:10.1017/jfm.2015.103.

Deka, H., Pierson, J.L. and Soares, E.J., 2019. "Retraction of a viscoplastic liquid sheet". *Journal of Non-Newtonian Fluid Mechanics*, Vol. 272, p. 104172.

Deka, H., Pierson, J.L. and Soares, E.J., 2020. "Retraction criteria of viscoplastic drops and sheets: Long-wave approximations". *Journal of Non-Newtonian Fluid Mechanics*, Vol. 284, p. 104352.

Deoclecio, L.H.P., Soares, E.L., Deka, H. and Pierson, J.L., 2021. "Bubble entrapment condition in bingham materials". *J, Non-Newtonian Fluid Mechanics*, Vol. 295, p. 104616.

EPE, 2022. "National energy balance 2022, final report (in portuguese)". Empresa de Pesquisa Energética EPE, Rio de Janeiro, epe.gov.br/sites-pt/publicacoes-dados-abertos/publicacoes/PublicacoesArquivos/publicacao-675/topico-638/BEN2022.pdf. Accessed 02 May 2023.

Farsoiya, P.K., Popinet, S. and Deike, L., 2022. "Direct numerical simulations of dilute gas transfer by breaking waves". *Physical Review Fluids*, Vol. 7, No. 11. doi:10.1103/physrevfluids.7.110506.

Fathi, S.J., Austad, T. and Strand, S., 2011. "Water-based enhanced oil recovery (eor) by "smart water":optimal ionic composition for eor in carbonates". *Ernery and Fuels*, Vol. 25, pp. 5173–5179.

Galusinski, C. and Vigneaux, P., 2008. "On stability condition for bifluid flows with surface tension: Application to microfluidics". *Journal of Computational Physics*, Vol. 227, No. 12, pp. 6140–6164. doi:10.1016/j.jcp.2008.02.023.

Gu, Q., Liu, H. and Zhang, Y., 2018. "Lattice boltzmann simulation of immiscible two-phase displacement in two-dimensional berea sandstone". *Applied Sciences*, Vol. 8, No. 9, p. 1497. doi:10.3390/app8091497.

Johansen, H. and Colella, P., 1998. "A cartesian grid embedded boundary method for poisson's equation on irregular domains". *Journal of Computational Physics*, Vol. 147, No. 1, pp. 60–85. doi:10.1006/jcph.1998.5965.

Lagrée, P.Y., Staron, L. and Popinet, S., 2011. "The granular column collapse as a continuum: validity of a two-dimensional navier-stokes model with a $\mu(i)$-rheology". *Journal of Fluid Mechanics*, Vol. 686, pp. 378–408.

Lenormand, R., Touboul, E. and Zarcone, C., 1988. "Numerical models and experiments on immiscible displacements in porous media". *Journal of Fluid Mechanics*, Vol. 189, pp. 165–187. doi:10.1017/s0022112088000953.

Limare, A., Popinet, S., Josserand, C., Xue, Z. and Ghigo, A., 2022. "A hybrid level-set / embedded boundary method applied to solidification-melt problems". doi:10.48550/ARXIV.2202.08300.

Liu, H., Valocchi, A.J., Kang, Q. and Werth, C., 2013. "Pore-scale simulations of gas displacing liquid in a homogeneous pore network using the lattice boltzmann method". *Transport in Porous Media*, Vol. 99, No. 3, pp. 555–580. doi:10.1007/s11242-013-0200-8.

Mora, P., Morra, G., Yuen, D.A. and Juanes, R., 2021. "Influence of wetting on viscous fingering via 2d lattice boltzmann simulations". *Transport in Porous Media*. doi:10.1007/s11242-021-01629-8.

Muggeridge, A., Cockin, A., Webb, K., Frampton, H., Collins, I., Moulds, T. and Salino, P., 2014. "Recovery rates, enhanced oil recovery and technological limits". *Philosophical Transactions of the Royal Society A: Mathematical, Physical and Engineering Sciences*, Vol. 372, No. 2006, p. 20120320. doi:10.1098/rsta.2012.0320.

Needham, R.B. and Doe, P.H., 1987. "Polymer flooding review". *J. Petroleum Tech.*, Vol. 39, pp. 1503–1507.

Nilsson, M.A., Kulkarni, R., Gerberich, L., Hammond, R., Singh, R., Baumhoff, E. and Rothstein, J.P., 2013. "Effect of fluid rheology on enhanced oil recovery in a microfluidic sandstone device". *Journal of Non-Newtonian Fluid Mechanics*, Vol. 202, pp. 112–119. doi:10.1016/j.jnnfm.2013.09.011.

Pierson, J.L., Magnaudet, J., Soares, E.J. and Popinet, S., 2020. "Revisiting the taylor-culick approximation: Retraction of an axisymmetric filament". *Phys. Rev. Fluids*, Vol. 5, p. 073602.

Popinet, S., 2009. "An accurate adaptive solver for surface-tension-driven interfacial flows". *Journal of Computational Physics*, Vol. 228, No. 16, pp. 5838–5866.

Popinet, S., 2015. "A quadtree-adaptive multigrid solver for the serre–green–naghdi equations". *Journal of Computational Physics*, Vol. 302, pp. 336–358.

Popinet, S., 2018. "Numerical models of surface tension". *Annual Review of Fluid Mechanics*, Vol. 50, pp. 49–75.

Salmo, I.C., Sorbie, K.S. and Skauge, A., 2021. "The impact of rheology on viscous oil displacement by polymers analyzed by pore-scale network modelling". *Polymers*, Vol. 13, No. 8, p. 1259. doi:10.3390/polym13081259.

Salmo, I.C., Zamani, N., Skauge, T., Sorbie, K. and Skauge, A., 2020. "Use of dynamic pore network modeling to improve our understanding of experimental observations in viscous oil displacement by polymers". In *Day 2 Tue, September 01, 2020*. SPE. doi:10.2118/200387-ms.

Shende, T., Niasar, V. and Babaei, M., 2021. "Pore-scale simulation of viscous instability for non-newtonian two-phase flow in porous media". *Journal of Non-Newtonian Fluid Mechanics*, Vol. 296, p. 104628. doi:10.1016/j.jnnfm.2021.104628.

Soares, E.J., Carvalho, M.S. and Mendes, P.R.S., 2005. "Immiscible liquid-liquid displacement in capillary tubes". *Journal of Fluids Engineering*, Vol. 127, No. 1, pp. 24–31. doi:10.1115/1.1852484.

Soares, E.J. and Thompson, R.L., 2009. "Flow regimes for the immiscible liquid–liquid displacement in capillary tubes with complete wetting of the displaced liquid". *Journal of Fluid Mechanics*, Vol. 641, pp. 63–84. doi:10.1017/s0022112009991546.

Soares, E.J., Thompson, R.L. and Niero, D.C., 2015. "Immiscible liquid–liquid pressure-driven flow in capillary tubes: Experimental results and numerical comparison". *Physics of Fluids*, Vol. 27, No. 8, p. 082105. doi:10.1063/1.4928912.

Taylor, G.I., 1960. "Deposition of a viscous fluid on a plane surface". *J. Fluid Mech.*, Vol. 9, pp. 8–14.

Taylor, G.I., 1961. "Deposition of a viscous fluid on the wall of a tube". *Journal of Fluid Mechanics*, Vol. 10, No. 02, p. 161. doi:10.1017/s0022112061000159.

Thomaz, J.E., 2001. *Fundamentos de Engenharia de Reservatório*, Vol. 2. Interciência, Rio de Janeiro:.

Thompson, R.L. and Soares, E.J., 2012. "Motion of a power-law long drop in a capillary tube filled by a newtonian fluid". *Chemical Engineering Science*, Vol. 72, pp. 126–141. doi:10.1016/j.ces.2011.12.027.

Tunio, S.Q., Tunio, A.H., Ghirano, N.A. and Adawy, Z.M.E., 2011. "Comparison of different enhanced oil recovery techniques for better oil productivity".

Zamani, N., Salmo, I.C., Sorbie, K. and Skauge, A., 2019. "Numerical study of polymer flow in porous media using dynamic pore network modelling". In *IOR 2019 – 20th European Symposium on Improved Oil Recovery*. European Association of Geoscientists & Engineers. doi:10.3997/2214-4609.201900120.

Zhang, C., Oostrom, M., Wietsma, T.W., Grate, J.W. and Warner, M.G., 2011. "Influence of viscous and capillary forces on immiscible fluid displacement: Pore-scale experimental study in a water-wet micromodel demonstrating viscous and capillary fingering". *Energy & Fuels*, Vol. 25, No. 8, pp. 3493–3505. doi:10.1021/ef101732k.

8. RESPONSIBILITY NOTICE

The authors are solely responsible for the printed material included in this paper.